ADVANCED MATERIALS INTERFACES
www.advmatinterfaces.de

Nano-spaced Gold on Glassy Carbon Substrate for Controlling Cell Behavior

Gaurav Chauhan, Alejandro Lujambio Ángeles, Everardo Gonzalez-González, Manish M. Kulkarni, Braulio Cardenas-Benitez, Martín Francisco Jiménez, Grissel Trujillo-de Santiago, Mario M. Alvarez, Marc Madou, and Sergio O. Martinez-Chapa**

This approach involves the synthesis of gold nanoparticles (GNPs) within the carbonizing photoresist (SU8) to achieve GNPs trapped glassy carbon (GNPs-GC) substrates. Surface size distribution and interparticle separation of GNPs is primarily controlled by changing the metal precursor concentration. Chemical stability and fabrication control are achieved by selecting sodium tetrachloroaurate ($NaAuCl_4$) over a more conventional aurochloric acid ($HAuCl_4$) as the gold precursor. Seeding of gold nuclei in a photocrosslinking polymer is a classical representation of simultaneous homogeneous and heterogeneous nucleation. GNPs growth during the carbonization process is tracked and explained using pertinent mechanisms. With the nanoparticle spacing ranging from 260 to 50 nm, GNPs-GC thin films are employed as interfaces for fibroblast cell adhesion. GNPs act as potential anchor points for cell adhesion and their nanoscale arrangement regulates the structural behavior of the cells. GNPs' density-dependent fibronectin physisorption significantly improves cell adhesion and proliferation. Intraparticle spacing around 160 nm offers ideal biointerface for fibroblast attachment and spreading. Fabrication of 3D GNPs composite carbon microelectromechanical systems is achieved as a demonstration of the studied GNPs-GC synthesis mechanism. Sub-micron patterning of GNPs-GC combined with its biofunctional nature presents vast opportunities in the field of bioelectronics, biophotonics, and lab/organ-on-a-chip technology.

1. Introduction

Nanopatterns of gold nanoparticles (GNPs) with controlled spatial arrangements have a wide range of application in optics, electronics, catalysis, and biomaterial science.[1–10] These patterns are typically created on surfaces like glass and silicon wafer using block copolymer micelle nanolithography.[11–13] Length of the block copolymer chains determines the regular spacing between the nanoparticles. Patterning of large and even curved areas is achieved by micro-contact deprinting method where polystyrene stamp is used to peel off GNPs-loaded block copolymer micelles.[14] From a biology perspective, micro- and nanopatterns are important for imitating the physiognomies of biological structures.[15–17] As a biomaterial, its nanoparticle spacing, topography pattern, and chemistry defines the nature of biological interaction.[18] Cellular response and phenotypes can be regulated by utilizing the ligand (such as the arginine–glycine–aspartic acid "RGD") receptor (such as integrins) pattern control at the biointerface.[11,19,20] Techniques reported above to

Dr. G. Chauhan, A. L. Ángeles, B. Cardenas-Benitez, M. F. Jiménez, Prof. M. Madou, Prof. S. O. Martinez-Chapa
School of Engineering and Sciences
Tecnologico de Monterrey
Av. Eugenio Garza Sada 2501 Sur, Monterrey, NL 64849, Mexico
E-mail: mmadou@uci.edu; smart@tec.mx

E. Gonzalez-González, Prof. G. Trujillo-de Santiago, Prof. M. M. Alvarez
Centro de Biotecnología- FEMSA
Escuela de Ingeniería y Ciencias
Tecnologico de Monterrey
Av. Eugenio Garza Sada 2501 Sur, Monterrey, NL 64849, Mexico

The ORCID identification number(s) for the author(s) of this article can be found under https://doi.org/10.1002/admi.202000238.

DOI: 10.1002/admi.202000238

E. Gonzalez-González, Prof. G. Trujillo-de Santiago, Prof. M. M. Alvarez
Departamento de Bioingeniería
Tecnologico de Monterrey
Av. Eugenio Garza Sada 2501 Sur, Monterrey, NL 64849, Mexico

Dr. M. M. Kulkarni
Centre for Nanosciences
Indian Institute of Technology Kanpur
Kanpur, Uttar Pradesh 208016, India

Prof. G. Trujillo-de Santiago
Departamento de Mecatrónica
Tecnologico de Monterrey
Av. Eugenio Garza Sada 2501 Sur, Monterrey, NL 64849, Mexico

Prof. M. Madou
Department of Mechanical and Aerospace Engineering
University of California Irvine
Engineering Gateway 4200, Irvine, CA 92697, USA

fabricate GNPs nanopatterns require a high level of precision and sophisticated protocols, which are costly and slow. The present manuscript reports the fabrication of gold nanopattern on glassy carbon (GC) substrate, where GNPs are nucleated by in situ reduction of gold precursor in a photocrosslinking polymer (SU8), and then grown into nanoparticles during carbonization (at 900 °C) to get GNPs-GC.

GC is chemically inert and an electrically conductive material (25 000 Ohm) composed of an amorphous 3D array of mainly chemically sp_2 bonded carbon atoms.[21] It is easy to fabricate by pyrolyzing precursors such as SU8 and polyacrylonitrile among other polymers.[22,23] It is widely used in carbon microelectromechanical systems (C-MEMS) such as for the fabrication of carbon interdigitated electrode arrays for redox amplification,[24,25] dielectrophoretic devices,[26] biosensors,[27] nanogap electrodes,[28] and supercapacitors[29] among many other applications. Being inert also entails limitations as chemical and biological sensing typically require physical or chemical attachments of reactive species on the GC surface. For this reason, several GC works involve surface functionalization schemes for biosensing by decorating the material´s surface by solvothermal deposition[30–35] and by electrodeposition in solution.[35,36] In particular, noble-metal nanoparticles (NPs), either by doping of or surface attachment to carbon films, have been extensively studied[35,37–41] because of their versatility, chemical stability,[42,43] and unique optical properties.[44] These NPs have also found application in microelectromechanical devices such as sensors,[45] medical devices.[46] GNPs, in particular, have attracted interest in the development of gold–carbon composites for non-enzymatic biosensing.[47–50] From an electronic and electrochemical perspective of GC, the surface presence of GNPs is important for enhancing its surface reactivity and binding sites for biomolecular surface functionalization.[39,47–49] A brief analysis of reported methods and applications for adding GNPs on GC surface is presented in (in Table S1 in the Supporting Information).

Here, we present a fabrication protocol which is chemically reliable, easily controllable for scaleup technologies with no additional step required for GNPs inclusion. This study is the first report of gold entrapped glassy carbon, aims at understanding the chemistry of gold precursor selection, in situ reduction inside the photocrosslinking matrix. It is further explained how we can stabilize and control this process for lithographically patterning of 3D features or MEMS. We explain the nucleation process and growth mechanisms involved in the nanoscale organization of GNPs in the carbonizing matrix. GC surfaces with controlled GNPs interparticle spacing, density, and size were used to culture human dermal fibroblasts. We report the effect of these substrate features on the attachment, spreading, and viability of cells.

2. Results and Discussion

2.1. GNPs-GC: Surface and Bulk Characteristics

The GNPs-GC fabrication is explained schematically in **Figure 1** and the details are presented in Section 4. The metrology results of the in situ synthesized GNPs-GC composite thin film are presented in this section. In **Figure 2**a–d, we illustrate the presence of GNPs at the surface of the GNPs-GC composite thin films. Due to the large atomic number difference between gold and carbon, the contrast in the high definition backscattered electron

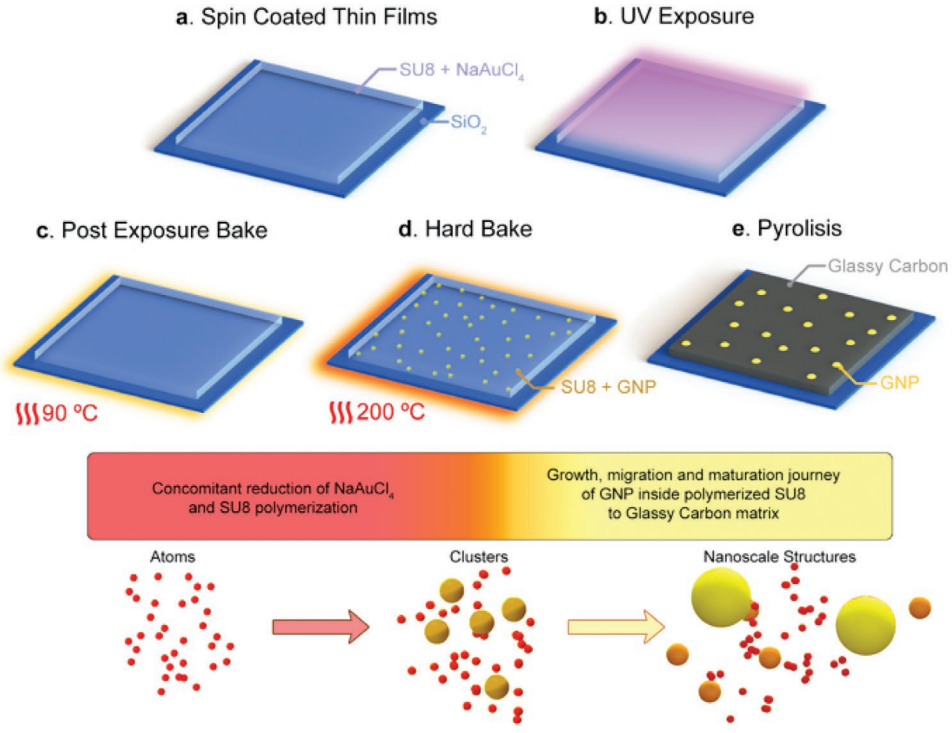

Figure 1. a–e) Schematic of the experimental setup and the steps involved in the fabrication of the GNPs-GC composite.

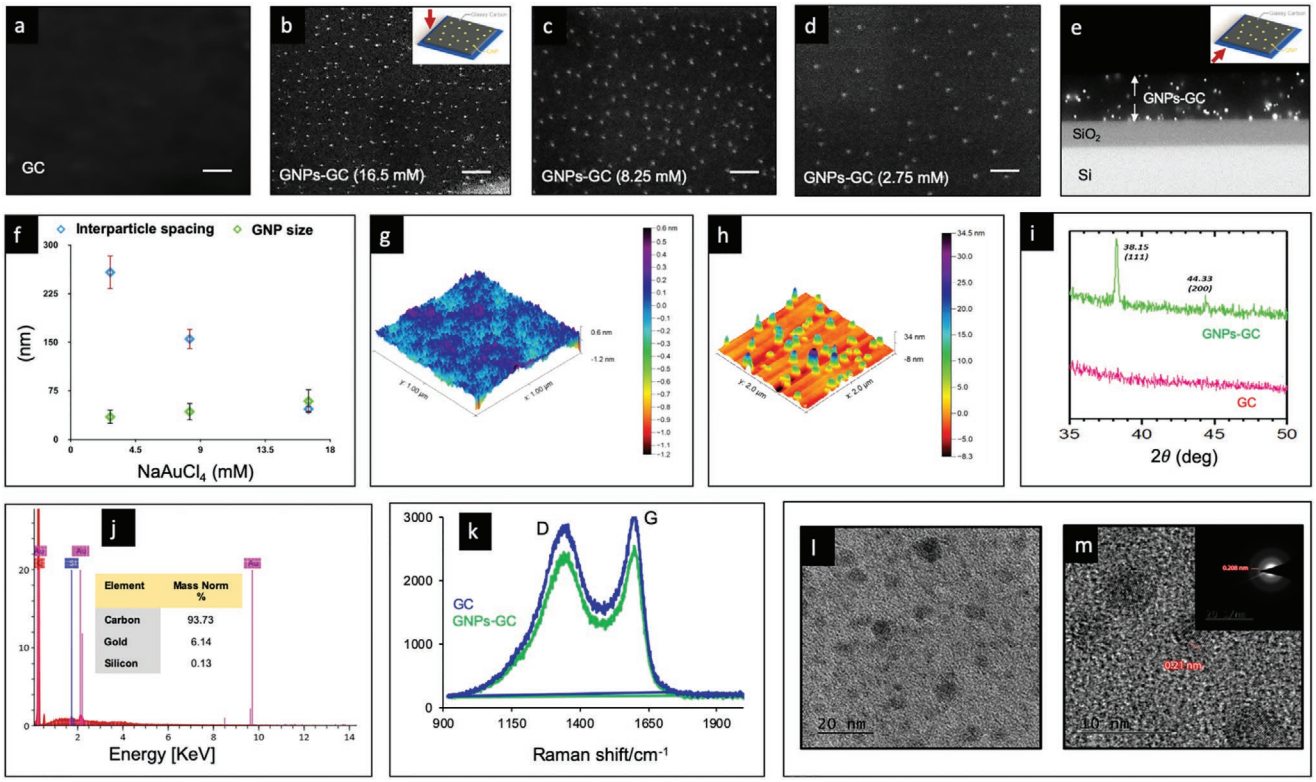

Figure 2. a–d) High definition backscattered electron emission image of the GNPs presents on the surface of GNPs-GC (constant film thickness 1 µm, 2.25 cm^2 surface area and exposure at 165 mJ cm^{-2}) with different $NaAuCl_4$ concentrations. ImageJ software is used to analyze these SEM images, scale bar = 200 nm. e) Transverse cut section of GNPs-GC thin film (8.25×10^{-3} M $NaAuCl_4$, 2 µm thickness) showing the presence of GNPs embedded in the bulk matrix. f) Effect of $NaAuCl_4$ concentration on GNPs size and spacing on the surface of GNPs-GC films (constant film thickness 1 µm and 2.25 cm^2 surface area). g) AFM image of pristine GC surface, surface roughness (Ra) is 0.39 nm. h) AFM image of GNPs-GC surface (8.25×10^{-3} M $NaAuCl_4$) with embedded GNPs. i) X-ray diffraction spectra showing the GNPs specific peaks in GNPs-GC spectra in contrast to GC spectra. j) EDS spectra of the GNPs-GC (8.25×10^{-3} M $NaAuCl_4$) surface with the elemental composition percentage. k) Raman spectra of GNPs-GC and reference GC exhibits a sharp D peak at ≈1350 cm^{-1} and G peak at ≈1580 cm^{-1}. l) High-resolution transmission electron microscopy images of GNPs present in the GNPs-GC matrix (8.25×10^{-3} M $NaAuCl_4$). m) Fringe distance of the crystalline GNPs with selected area diffraction pattern (SAED, inset).

emission images clearly demonstrates the presence of uniformly located GNPs at the surface of the glassy carbon. Cross-section scanning electron microscopy (SEM) imaging further reveals the presence of GNPs in the bulk/matrix of GNPs-GC substrate as well (Figure 2e). Characteristics of GNPs present in the matrix along the depth depends on the thickness of the films (specified in the following sections). Particle size and density of the in situ synthesized GNPs is highly dependent on the concentration of the gold precursor ($NaAuCl_4$) (Figure 2f). Interparticle distance of embedded GNPs changes from around 258 ± 27 to 47 ± 9 nm as the $NaAuCl_4$ concentration increased from 2.75 to 16.5×10^{-3} M. Increasing gold precursor concentration also effect the size of GNPs present on the surface with an increase from 36 ± 8 to 62 ± 11 nm (Figure 2f). A strict control over the composition and process variables (as mentioned in Section 4) is required to achieve right GNPs distribution. GNPs-GC fabrication is highly reliant on parameters such as crosslinking of photoresist matrix and carbonization protocol, as explained in the nucleation and growth section. Atomic force microscopy (AFM) reveals the topology differences between pristine GC and GNPs-GC surfaces (Figure 2g,h). From the AFM images we clearly see the presence of gold nanostructures fixed at and embedded in the surface of the carbon matrix.

In the X-ray diffraction (XRD) spectra, we observe the presence of face centered cubic (FCC) reflections at 38.1° and 44.3° associated with the GNPs (Figure 2i). We also performed energy-dispersive X-ray spectroscopy (EDS) to check the composition of the thin film material and confirmed the presence of gold, carbon, and silicon (Si is the carbon film substrate) (Figure 2j). The complete absence of chlorine in the EDS spectra indicates the complete reduction of the GNPs precursor salt. From the Raman spectra of GNPs-GC we recognize the characteristic glassy carbon peaks, unchanged from those for pristine GC, so we can conclude that the carbon microstructure remains unchanged, after the in situ synthesis of gold nanostructures (Figure 2k). Unlike metals such as nickel, iron, and silicon, that catalyze the transformation of the carbon microstructure during pyrolysis toward a more graphitic material,[51–53] gold does not and only pristine glass like carbon results.

High-resolution TEM (HR-TEM) imaging of the GNPs embedded in the GC matrix was performed by scratching the thin film surface with a diamond cutter tip and suspending the collected material in ethanol by sonication for 20 min. The HR-TEM images reveal that the GNPs are less than 10 nm in size, which is caused either by steric confinement within the hardening polymer precursor or within the GC (Figure 2l) (depending on the timing

of the nucleation and growth mechanisms involved, detailed in the following sections). In either case, the nanostructure migration is restricted, limiting the further GNP growth. GNPs specific crystalline peaks are also confirmed by the HR-TEM and selected area diffraction (SAED) results (Figure 2m). In the HR-TEM micrograph, we show a GNP with its (200) lattice fringes, while in the SAED, the rings related to the (111) and (200) reflections from nanoparticles are displayed in Figure 2m (inset). This crystallinity data of the GNPs is in agreement with the XRD results from Figure 2i; confirming FCC reflections of GNPs located at 38.1° (111) and 44.3° (200). Elemental mapping of a section of the GNPs-GC composite matrix with STEM indicates gold embedded in a carbon matrix (see Figure S1 in the Supporting Information).

2.2. Concomitant Photopolymerization and $NaAuCl_4$ Reduction

The photopolymerization of SU8 and the simultaneous reduction of the gold salt in that polymer matrix figures as the most important step to obtain an intermediate composite that results in GNPs embedded in the GC upon further pyrolysis. This particular step is responsible for: a) formation of nucleation sites for gold within the photocrosslinked polymer matrix, and b) the entropic control for intraparticle ripening.

The understanding of the driving force for the reduction of the gold precursor and for the initial GNPs nucleation during the SU8 crosslinking phase is crucial for the control of size and distribution of the GNPs. A gold salt reduction mechanism proposed by Shukla and co-workers[38] emphasizes the important role of the strong photoacid [$(Ar)_3S^+SbF^-_6$], that is, an onium salt that decomposes to form a Lewis acid (hexafluoroantimonic acid, $-H^+SbF6^-$), during post exposure bake (PEB) of the chemically amplified SU8 photoresist.[54] In this scenario, the Lewis acid is responsible for both the reduction of the ionic gold and for the cationic polymerization of the SU8.[38] Our finding also points toward the role of the photoacid but the most important component for the chemical reduction of the gold chloride is cyclopentanone, the solvent of the SU8 photoresist (**Figure 3**). UV exposure of the photoresist initiates the epoxy groups protonation (cationic H^+), which is followed by the ring opening of these groups, resulting in the formation of carbocations, which further attack more epoxy rings propagating the crosslinking reaction of the SU8 molecules (Figure 3a).

Our study reveals the simultaneous consumption of cationic H^+ for the tautomeric conversion of cyclopentanone into enolic ($-OH^-$) intermediates, which initiates the reduction of the gold precursor followed by an equilibrium disproportionation reaction into zero-valent gold ions (required for GNP's nucleation) (Figure 3b).[55,56]

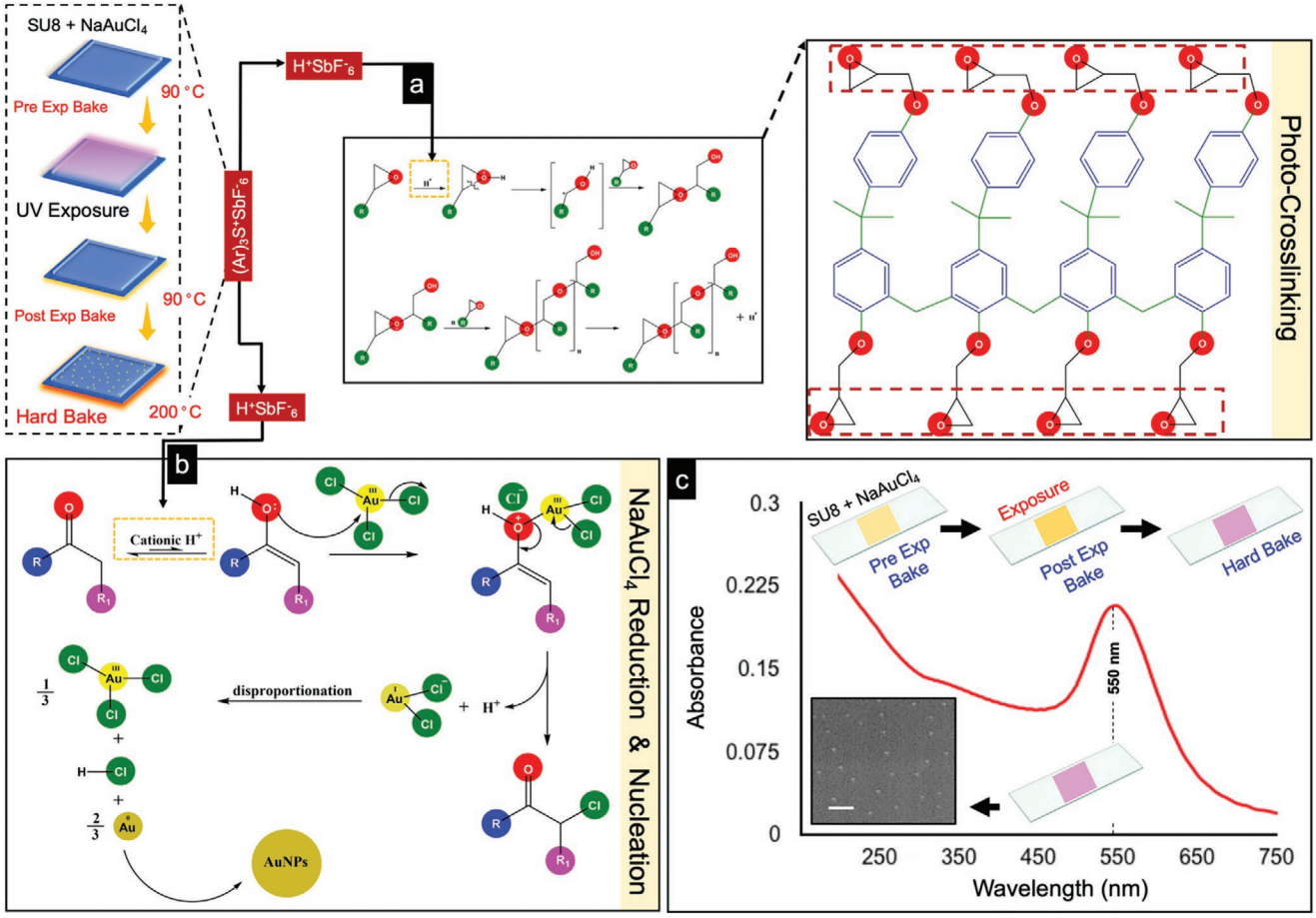

Figure 3. a) Activation of photoacid generator results in cationic polymerization reaction (as explained by Shukla et al.[38] and similarly, by Markham et al.[55] in photoresist and b) simultaneous reduction reaction with metallic salt precursor in the same composition. c) GNPs nucleated in the thin films after hard bake of 8.25×10^{-3} M precursor composition (inset SEM image scale bar = 200 nm).

2.3. Classical GNPs Nucleation and Controlling Factors

The reduction of the gold precursor is followed by the nucleation or seeding of small templates for crystal growth into GNPs.[57] In Figure 3a,b the reduction of the gold precursor during UV exposure and hard bake is illustrated. These two steps generate reduced gold ions in the polymeric matrix. These reduced gold ions in the polymer matrix then undergo nucleation, with the rate of the nucleation a function of the availability of free gold ions.[58–60]

Experimentally, the presence of GNPs is first observed during the hard bake step. When the temperature first reaches 180–200 °C, the yellowish transparent thin film changes to a light purple color, indicating the GNP formation in the crosslinking SU8 matrix. After 1 h of hard bake uniformly distributed GNPs with an average size of 30 nm are observed. Figure 3c shows the UV–vis absorption spectra of hard baked sample with characteristic GNPs absorption peak at 550 nm and SEM image (inset) showing the presence of uniformly distributed GNPs. The concomitant reduction of the gold salt and the crosslinking of the SU8 matrix, and the subsequent hard bake provide a stable platform of crosslinked SU8 thin films with embedded GNPs, ready for the next step of pyrolysis (Figure 1). The pyrolysis at 900 °C of the hard baked material does not only carbonize the crosslinked SU8 into GC, but it also drives the next step in the journey of the GNPs growth while producing fullerene like structures within the matrix.[23] This last step involves the migration and maturation of the GNPs inside the continuously hardening and more and more constricting carbon matrix. This transformation of $NaAuCl_4$ containing SU8 thin films into GNPs-GC, requires further explanation.

2.4. Kinetics of Reduction and Nucleation

The very first step for an understanding of the gold nucleation process is to define the chemistry and the kinetics involved in the precursor reduction. The photoacid-dependent gold chloride reduction is controlled by the cyclopentanone solvent, which is a relatively weak reducing agent compared to the commonly used sodium citrate and sodium borohydride.[61–64] It is a challenge to suggest reaction intermediates that possibly play a role in this non-aqueous reduction process. Based on bond length calculations between gold atoms, Yao et al., postulate that gold can be reduced in either a monomer or in a dimer/trimer mode as symbolized in the following Equations (1) and (2).[65]

$$M^{x+} + xe \rightarrow M^0$$
$$M^0 + M_n^0 \rightarrow M_{n+1}^0 \quad (1)$$

$$M^{x+} + e \rightarrow M^{(x-1)+}$$
$$M^{(x-1)+} + M^{(x-1)+} \rightarrow M_2^{(2x-2)+}$$
$$M_2^{(2x-2)+} + xe \rightarrow M_x \quad (2)$$

As we saw above, the photoacid influx is a key factor that determines the initiation and the kinetics of the gold nucleation.[66,67] The UV exposure dose governs the amount of photoacid in the exposure step and indirectly it also controls the balance of precursor versus reducing agent concentration. The effect of the exposure time on the average size and surface spacing of the GNPs after hard bake was estimated and as shown in **Figure 4**a,b, there is an inverse relationship between exposure time (dose) and particle size. This study was performed with exposure doses restricted to the experimental limits of typical carbon MEMS fabrication parameters (50–200 mJ cm^{-2}).

Exposure time/dose and the $NaAuCl_4$ concentration are the key parameters offering the control one can exert over the extent of uniform nucleation and subsequent growth of GNPs. The kinetics of gold reduction and nucleation thus involve both diffusion control in a crosslinking/photopolymerizing matrix and the free initial concentration of metal ions.

Consequently, the two dynamic factors we need to model are nucleation and progressing photopolymerization. According to the LaMer model, an increased free metal ion concentration in the reaction phase results in faster nucleation rates followed by growth.[60,68] We start with describing the rate of nucleation by Arrhenius type Equations (3a) and (3b).

$$\frac{dN}{dt} = A\, exp\left(-\frac{\Delta G_{crit}}{k_B T}\right) \quad (3a)$$

$$\frac{dN}{dt} = A\, exp\left(-\frac{16\,\pi\gamma^3 v^2}{3k_B^3 T^3 \ln(S)^2}\right) \quad (3b)$$

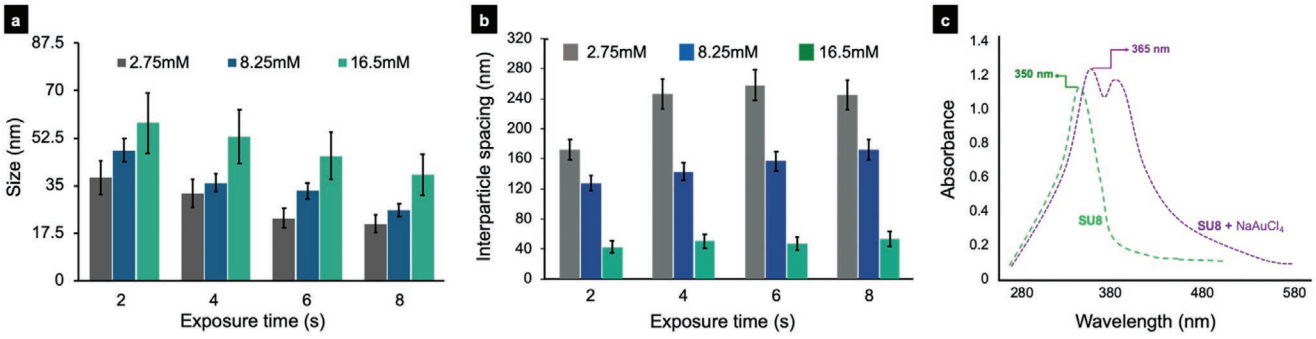

Figure 4. Observed a) GNPs sizes and b) interparticle spacing at different exposure doses and different $NaAuCl_4$ concentrations (constant film thickness 1 µm, 2.25 cm^2 surface area and exposure time of 2 s (55 mJ cm^{-2}), 4 s (110 mJ cm^{-2}), 6 s (165 mJ cm^{-2}), 8 s (220 mJ cm^{-2}). c) UV–vis spectra of SU8 and SU8 + 10×10^{-3} M $NaAuCl_4$ showing an overlap in the 350 nm wavelength region.

where, N is the number of nanoparticles, ΔG_{crit} is known as the critical energy which is the minimum energy requirement for the nanoparticle nucleation to happen, A is a proportionality constant, ν is the molar volume, T is the temperature, k_B is the Boltzmann constant, γ is the surface energy of the crystal, and S is the level of supersaturation. Supersaturation is defined as $[M]/[M]_0$, where $[M]_0$ is the equilibrium monomer (minimal building unit of a nanoparticle) concentration of the bulk solid. From Equations (3a) and (3b) one recognizes the huge effect of the supersaturation parameter on the nucleation rate: a change from $S = 2$–4 results in an almost $\approx 10^{70}$ times increased nucleation rate.[57,69] The nucleation growth is controlled by the diffusion of gold ions to the initial Au seeds, and faster diffusion results in bigger particles and less uniform particle spacing.

Now comes the second dynamic parameter into play, that is, the photocrosslinking rate, which in turn is impacted by two important subfactors. The first subfactor is related to the consumption of photoacid by the reduction of the available gold precursor as described earlier in Figure 3a,b. The acid consumed in this reaction cannot be used anymore for the competing SU8 crosslinking reaction and this results in a lower degree of photocrosslinking.[64,70] The second subfactor is related to the fact that the absorption spectrum of $NaAuCl_4$ at 360 nm overlaps with that of SU8 as shown in Figure 4c. An increased concentration of gold precursor thus also negatively affects the degree of crosslinking of the SU8 polymer by reducing the available photons for the activation of the acid.[71] Hence, an increased gold precursor concentration results in less crosslinking of the SU8, which results in faster diffusion of free gold ions and small gold nuclei within the polymer matrix to assist the growth of bigger nanoparticles. These considerations again explain the increase in the nanoparticle size at a higher $NaAuCl_4$ concentration.

The hard bake step removes all remaining casting solvent (cyclopentanone) from the polymer matrix and anneals the films.[72] Due to nucleation and growth constraints in the hardening polymer matrix, presence of gold clusters and considerably small GNPs is not surprising.[73] To analyze those growth constraints in the hardening photoresist we first consider the thermodynamics of nucleation in a classical homogenous system, where the total free energy of a nanoparticle (ΔG or ΔG^{homo}) is given by Equation (4), where ΔG is a direct function of the free energy of the bulk crystal (ΔG_v) given in Equation (5).

$$\Delta G = 4\pi r^2 \gamma + \frac{4}{3}\pi r^3 \Delta G_v \tag{4}$$

$$\Delta G_v = -\frac{k_B T \ln(S)}{\nu} \tag{5}$$

ΔG_{crit} determines the critical GNP radius (r_{crit}) in Equation (7), that is, the minimum size a gold particle must reach without it being possibly redissolved.

$$\Delta G_{crit} = \frac{4}{3}\pi\gamma r_{crit}^2 = \Delta G_{crit}^{homo} \tag{6}$$

$$r_{crit} = \frac{-2\gamma}{\Delta G_v} = \frac{2\gamma\nu}{k_B T \ln(S)} \tag{7}$$

Our observations suggest that the crosslinking SU8 matrix has a direct effect on the surface energy of the spherical gold particles embedded in it, with the crosslinking polymer network lowering the surface energy γ values. Those lower surface energy values drag down ΔG^{homo} and ΔG_{crit}, leading to a smaller critical radius for particles to survive in the system. This explains the results obtained by TEM as shown in Figure 2l,m, where GNPs less than 6 nm are observed in the bulk of the GC matrix.

In the bulk of the complex and constantly changing polymer matrix, the GNPs synthesis follows the above classical "homogeneous pathway" to crystallization. However, in the case of thin films we further adjusted the model. Heterogeneous nucleation is a result of structural inhomogeneities[74] and these include the presence of defects and interfaces (phase boundaries) that must be taken into account. The minimum free energy requirement for heterogeneous particle nucleation ΔG_{crit}^{hetero} is the product of the minimum free energy for homogeneous nucleation and a function Φ of the contact angle with that interfaces as given by Equation (8).

$$\Delta G_{crit}^{hetero} = \Phi \Delta G_{crit}^{homo} \tag{8}$$

When a stable interface is available, the effective surface energy is lower, thus diminishing the free energy barrier and facilitating nucleation (heterogeneous nucleation) as depicted in **Figure 5**a,b. In the film model applicable in the current case, we distinguish two types of heterogeneous nucleation at two different interfaces, that is, the interface of the SU8 with the SiO_2 coated Si wafer and the one associated with the slightly overexposed top SU8 surface. Since the SU8 compositions are spin coated on the silicon wafers, the top silicon oxide layer acts as the first stable interface. Hence, bigger GNPs are expected to be present at this interface because of faster nucleation (Figure 5e,f). A second interphase responsible for heterogeneous nucleation is due to the non-uniform photocrosslinking within the polymer matrix (Figure 5d,g). The concentration of the gold precursor and the thin film thickness are the two most prominent factors affecting the uniformity of photocrosslinking along with the surface distribution of GNPs (Figure 5c). The crosslinking gradient in the SU8 film is given by Beer–Lambert's law in Equation (9).

$$I(z) = I_0 e^{-\alpha c z} \tag{9}$$

where z is the thickness of the film, α is its absorptance, c is the concentration of the photon absorbing chemical species in the resist (i.e., both SU8 and the salt precursor as evident from Figure 4c) and, I_0 is the total photon flux at the top of the resist film. That this type of heterogeneous nucleation occurs in the present SU8 thin films was confirmed by experiments in which we changed c (from 2.75 to 8.25×10^{-3} M) and z (from 1 μm to 2 μm). As expected, lower values for c and z favor a more uniform crosslinking of the photoresist with exceptionally large GNPs (90–140 nm, oblong or oval shapes) at the silicon oxide interface demonstrating the faster and easier nucleation at that sharp interface. The cross-sectional SEM images in Figure 5e–g further affirm our explanation for more heterogeneous nucleation when using higher c and z (also explained in Figure 5d), with the probability of heterogeneous nucleation changing along the thickness of the film.

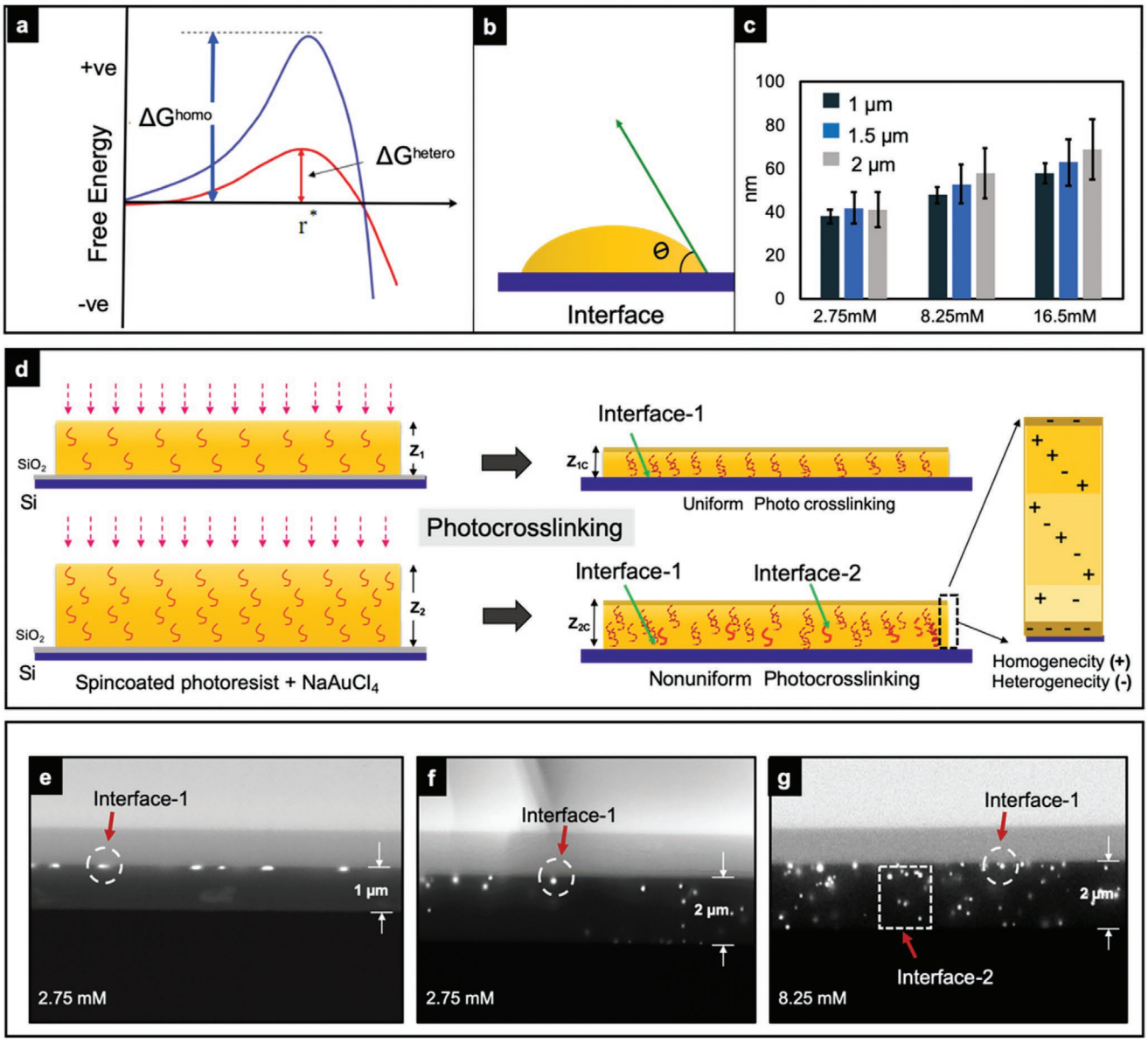

Figure 5. a) Free energy plot for homogeneous and heterogeneous nucleation, b) illustration of interphase contact angle in heterogeneous nucleation mechanism. This interface promotes nucleation because of wetting-contact angles greater than zero between phases facilitate particles to nucleate. c) Effect of GNPs-GC film thickness and $NaAuCl_4$ concentration on surface distribution of GNPs. d) Pictorial representing the effect of film thickness "z" on the photocrosslinking uniformity of two similar resist compositions, and the chances of homogenous (+) and heterogeneous (–) nucleation along the film thickness. e–f) Cross-sectional SEM images of GNPs-GC films fabricated with different precursor concentrations (2.75 and 8.25×10^{-3} M), thickness (1 and 2 μm), and exposure at 165 mJ cm^{-2}.

2.5. Selection of Stable Gold Precursor

In micro- and nano-electromechanical systems (MEMS and NEMS) a high level of photoresist crosslinking control is required to obtain structural features with ultra-fine precision. Hence, any transformation or instability of a photoresist before the external triggering of the crosslinking is highly undesirable. This requirement makes the selection of the correct gold precursor crucial since both the SU8 crosslinking and the GNPs nucleation requires an externally triggered and well-controlled acidic environment. This justifies the selection of the sodium salt of gold chloride ($NaAuCl_4$) over $HAuCl_4$, as a gold precursor mix with SU8.[75] According to the mechanism illustrated in Figure 3, an exposure-controlled H^+ environment is required for both photocrosslinking and gold chloride reduction, thus the presence of H^+ (from $HAuCl_4$) is undesirable as it would create an auto-initiated pre-exposure instability, resulting in uncontrolled SU8 crosslinking and reduction of gold chloride. Experiments were performed to compare the stability of SU8 + $NaAuCl_4$ and SU8 + $HAuCl_4$. The evidence is clear that SU8 + $HAuCl_4$ causes hydrogen salt induced crosslinking and concomitant gold chloride reduction to unstable gold particles

(see Figure S2 and S3 in the Supporting Information). The protons in the SU8 + $HAuCl_4$ mix obviate the need of exposure as the reaction can even occur in dark. In contrast, an SU8 + $NaAuCl_4$ mix remains stable in the dark, but daylight exposure initiates both photocrosslinking and gold chloride reduction (in accordance with the mechanism explained in Figure 3). The light induced crosslinking and gold chloride reduction with the SU8 + $NaAuCl_4$ mix occur at a much lower rate compared with that of the SU8 + $HAuCl_4$ mix. The change in color of SU8/$NaAuCl_4$ or SU8/$HAuCl_4$ solutions represents a first and simple indication of ongoing chemical changes; these changes are then further confirmed by SEM for the presence of gold nanostructures (see Figure S2 and S3 in the Supporting Information).

2.6. GNPs Growth during Carbonization/Pyrolysis

We analyze what happens with the GNPs during pyrolysis of the SU8 photoresist. The initial phase of pyrolysis below 500 °C contributes toward the dehydration and the removal of halogens from the original polymeric framework. A significant polymer shrinkage is observed above 500 °C because of hydrogen, oxygen, and nitrogen elimination. After reaching the final pyrolysis temperature of 900 °C, a dwell time of 60 min ensures complete carbonization. During the carbonization process, the GNPs growth is exposed to the thermochemical decomposition and the accompanying shrinkage of the polymer matrix. The GNPs growth inside this evolving polymer matrix depends on the reaction rate at the nanometal surface and on the diffusion of gold monomers inside the matrix toward the growing GNPs. Whereas, the gold monomer diffusion is enhanced by the heating of the polymer to 900 °C, the simultaneously carbonizing matrix opposes this diffusion. When a balance between these two is achieved, the GNPs become fixed within the carbonizing matrix.

Frame-by-frame analysis of the GNPs growth at various stages of the pyrolysis process is important. The usual carbonization protocol consists of ramping the temperature at a rate of 4.5 °C min^{-1} till 300 °C and 2.5 °C min^{-1} between 300 and 900 °C (with or without 60 min of dwell time at 300 and 900 °C) as shown in **Figure 6**. We inspected the GNPs size variations in the carbonizing polymer matrix upon imposing four different variations of this pyrolysis protocol (after hard baking, Figure 6a). In a first protocol, we inspect the GNP size distribution after reaching 300 °C without imposing a dwell time. The particle size distribution analysis from the SEM images in this case clearly reveals a bimodal size distribution one size centered around 54 nm and another around 230 nm as shown in Figure 6b,b*. In a second protocol, a 60 min dwell time was imposed after reaching 300 °C and this resulted in a single narrow particle size distribution around 45 nm (±6 nm) in Figure 6c. Similarly, in a third and fourth protocol, respectively, the particle size distribution after reaching 900 °C and no dwell time shows two broad distribution patterns centered around 49 and 158 nm as shown in Figure 6d,d*,e, whereas when adding a 60 min dwell time after reaching 900 °C results again in a single distribution pattern around 52 nm (±4 nm) as shown in Figure 6e. It is quite evident from the data that a well-defined GNP growth mechanism evolves throughout the pyrolysis process and that the details of the heating profile play an important role in controlling the penultimate particle size distribution of GNPs embedded in the GC matrix. Multiple growth mechanisms may contribute to the transformation of the GNPs in the carbonizing SU8 matrix as shown in Figure 6f–i: Ostwald ripening,[76] migration and coalescence,[77] size focusing,[78,79] and digestive ripening.[80]

When the crystallizable monomer (a product of gold salt reduction) concentration reaches a critical level (significantly above its equilibrium solubility), a burst of nucleation occurs. These monomers condense into nuclei and further contributes to the nanocrystal growth.[60] Our observations suggest that in the current case both Ostwald ripening and nanoparticle coalescence do occur during the heating ramp phase, where temperature is rising at a constant rate.[81] In Ostwald ripening atoms or small clusters of atoms diffuse from smaller to larger nanoparticles (Figure 6f). The phenomenon is based on the solubility change of nanoparticles as described by the Gibbs–Thomson relation Equation (10).[82,83]

$$C_r = C_b\, e^{\frac{2\gamma}{rk_BT}} \tag{10}$$

In the very initial heat ramp up to 300 °C, small sized GNPs (≈5 nm) grow in a diffusion limited step in relative defect free regions of the pyrolyzing matrix, hence their growth mechanism is restricted to Ostwald ripening.[76] Dissolution of GNPs during heating is another factor to consider as it will specifically favor the solubility of comparatively smaller sized GNPs, hence supporting this ripening mechanism.[84,85] For bigger GNPs in the polymeric framework, nanoparticle migration followed by coalescence is the more likely growth mechanism. The migration of GNPs may be assisted by regions in the carbonizing matrix where the number of structural defects created before and during the nucleation and previous particle maturation inside the crosslinking matrix is larger. Factors including the earlier introduced heterogeneous photocrosslinking and the size of the nanoparticle itself contribute to these structural defects that support migration-dependent coalescence. In Figure 6g, we illustrate how this growth mechanism for larger particles is supported by the fact that the overall number of GNPs decreases as their average diameter increases. Hence, the GNPs size distribution is bimodal with two different ranges, one centered around 55 nm (Ostwald ripening for GNPs < 10 nm) and one centered around 230 nm (migration and coalescence for GNPs > 25 nm).

Particle size focusing is observed during the 300 °C with 60-min dwell time pyrolysis protocol along with the digestive ripening of the largest GNPs resulting in a single particle size distribution pattern centered around 45 nm. Size focusing occurs when nanostructures present in the system are all slightly larger than the critical size,[78,79] under these conditions, the smaller nanocrystals in the distribution grow faster than the larger ones (Figure 6h). A theoretical description of the latter mechanism clarifies how a sufficiently high monomer concentration drives a decrease in the polydispersity of the particles even as their average size increases.[79] This explanation is limited to the medium sized GNPs (10-20 nm) present in the matrix, where the high monomer production is managed by the negative growth rate (dissolve) of small GNPs (<10 nm) and gold clusters. In digestive ripening we see the opposite of the

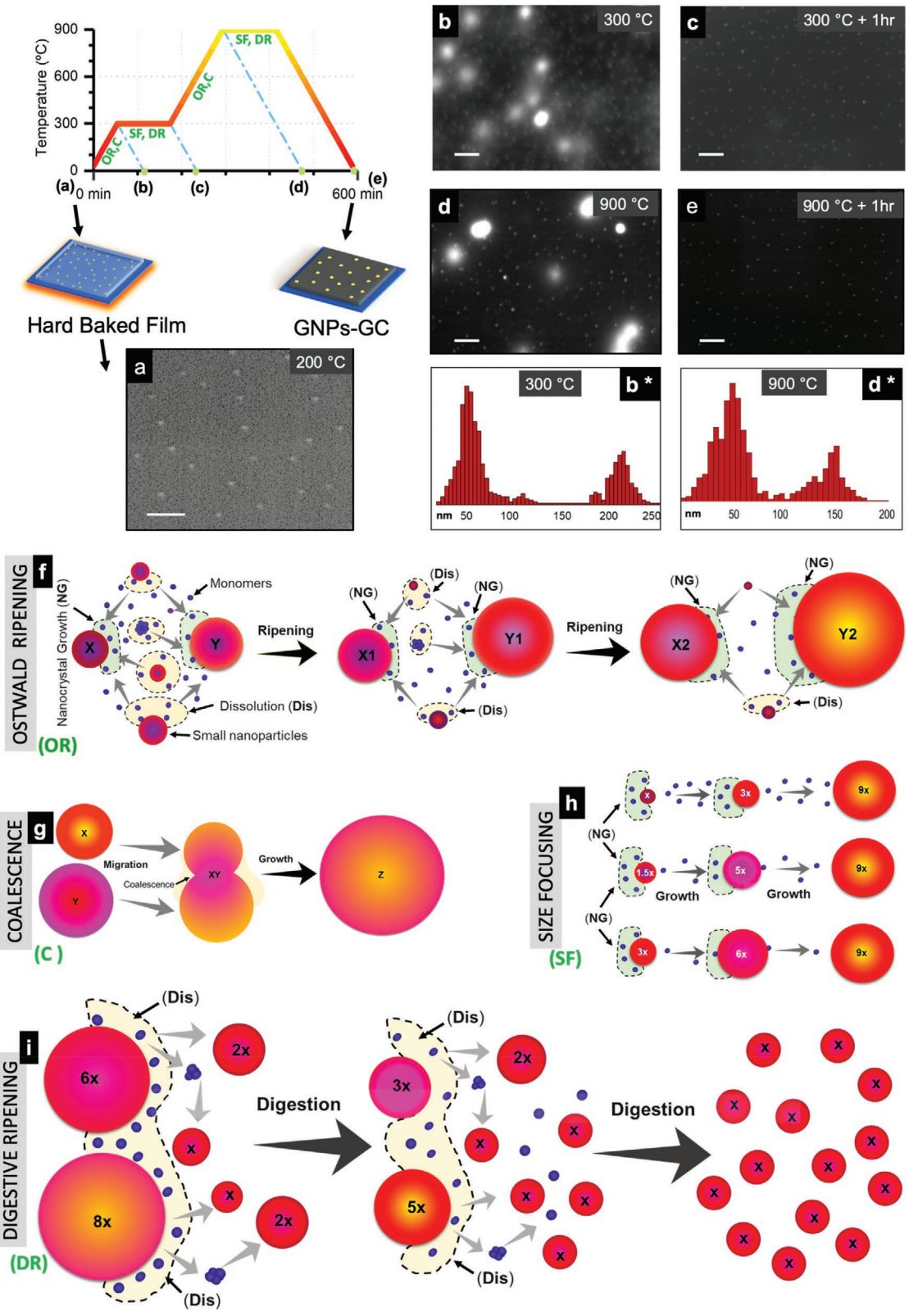

Figure 6. Growth of GNPs during the process of pyrolysis using a programmed heating ramp and dwell time. a) SEM images hard baked sample and b–e) carbonized samples after pyrolysis protocols reaching different temperatures with and without any dwell times. b*,d*) size distribution graph of SEM images (b) and (d), respectively (scale bar = 200 nm). f–i) GNPs growth mechanism followed during the entire carbonization in the pyrolysis process.

Ostwald ripening process at work.[80] Controlled again by the surface energy (Equation (10)) this process involves the dissolution of large GNPs to form smaller nanoparticles (Figure 6i). Hence, a dwell time after a temperature ramp provides a period over which both these mechanisms achieve a more uniform single GNPs distribution (45 nm) in the carbonizing matrix.

The GNPs growth is observed in the third pyrolysis protocol, where no dwell time is provided after ramping up to 900 °C is, as in the first protocol, based on Ostwald ripening and coalescence. This results in a very high percentage of small sized GNPs (<10 nm) that undergo Ostwald ripening with one associated distribution peak in the now very stable[23,86] carbonized matrix. Here also, migration and coalescence result in a second distribution peak of large GNPs, indicative of the presence of structural defects at this stage of the carbonization process. Finally, a unimodal GNP growth regime is observed in protocol four, where the size focusing, and digestive ripening mechanism dominate the growth process owing to another dwell period of 60 min.

2.7. Carbon-MEMS Fabrication and Demonstration of the Proposed GNPs-GC Synthesis Mechanism

The above analysis concerns non-patterned films only, but lithographically patterning 3D features in gold precursor-loaded SU8 films is still a challenge. Non-uniform crosslinking of the resist caused by the gold precursor composite photoresist presents a big hurdle for obtaining traditional 3D MEMS or 3D C-MEMS while maintaining good line-width resolution. Indeed, wet development of the SU8 patterns after PEB exploits the variation in molecular weight of the crosslinked polymer caused by the exposure to an image on a mask. To print that mask image with high fidelity it is very important to achieve the highest possible crosslinking contrast, obviously the crosslinking induced by the gold salt precursor interferes with that process (see the mechanism in Figure 3). Based on the explanation we provided for reduced photon exposure efficiency in the gold salt-loaded photoresist (see Figure 4c and Equation (9)) we resolved this issue with two different strategies. The first approach is to optimize the photoacid supply in the $NaAuCl_4$ containing photoresist. Our proposed mechanism for gold salt reduction suggests that the cationic photoinitiator present in the SU8 (supplied by MicroChem) is utilized for this additional task. Under standard experimental MEMS conditions, the photoinitiator concentration is actually not high enough to provide enough photocrosslinking contrast in the wet development step of a $NaAuCl_4$ containing photoresist. Thus, increasing the initial photoinitiator concentration is a first suggested solution to the contrast problem.[75] Specifically, our study revealed that at 8.25×10^{-3} M $NaAuCl_4$ concentration, the SU8 photoresist does not survive the wet development step but an addition of photoinitiator "PI" in a **2** ($NaAuCl_4$):**1** (PI) molar ratio solved this problem. Using this new SU resist formulation, interdigitated electrodes with a minimum feature size of 10 μm were successfully developed using standard SU8 processing parameters (**Figure 7**). A second work around procedure is based on increasing the exposure dose (two to three times as compared to traditionally suggested[87]) of the gold salt-loaded SU8. Unfortunately, this technique is limited to resist formulations with very low concentrations of gold precursor salt (2.75×10^{-3} M) only. The procedure is based on a more complete photoinitiator activation by the extra number of photons supplied, but because the amount of photoinitiator in the procured SU8 is low, increased exposure can only support very low $NaAuCl_4$ concentrations.

2.8. Fibronectin Adsorption and Cell-Culture Experiments

Fabricated GNPs-GC surfaces are further explored as a cell scaffold. The cell adhesion and morphology of dermal fibroblasts were found to be influenced on the interparticle distance, size, and density of GNPs on GC surfaces. GNPs-GC substrates were functionalized with fibronectin (FN) by physisorption, which was assisted by the electrostatic interaction between GNPs and the FN protein. This functionalization was conducted to enhance cell adhesion as explained in **Figure 8**a. BCA assay revealed the fibronectin adsorbed concentrations per 1×1 cm^2 films surface as: GC (0.015 ± 0.004 mg mL^{-1}), GNPs-GC 2.75×10^{-3} M (0.032 ± 0.009 mg mL^{-1}), 8.25×10^{-3} M (0.086 ± 0.012 mg mL^{-1}), and 16.5×10^{-3} M (0.108 ± 0.016 mg mL^{-1}). Cell attachment and proliferation rates studies with adult human dermal fibroblasts expressing green fluorescent protein cells (GFP-HDFa) reveal an overall direct proportionality between the number of cells attached and density of GNPs (Figure 8b,c). In the case of non-fibronectin coated surfaces (control), GNPs served as anchorage points for cell adhesion and reducing the interparticle distance between GNPs upon increasing the gold precursor concentration results in a higher number of cell attachment. Decreasing surface GNPs density with increasing particle size at 16.5×10^{-3} M precursor concentration (when compared to 8.25×10^{-3} M surfaces) resulted in a lower number of cell anchor points.[88] This effect is observed with a nonsignificant decrease in relative cell attachment observed at 16.5×10^{-3} M surfaces. Pristine GC surface with no fibronectin gives a poor surface cell adhesion.

When compared with control surfaces, FN surfaces show a significantly higher attachment and proliferation rate of GFP-HDFa cells (Figure 8b,c). Cell attachment on FN surface is directly related to the concentration of protein adsorbed on the surfaces. Figure 8b shows that surfaces functionalized with FN presented higher cell coverage than the non-functionalized control surface. Further, in FN surfaces, GNPs-GC surfaces show a significantly higher cell-coverage area with respect to pristine GC. Also, cell-coverage area is proportional to GNPs density on GNPs-GC surfaces. The interparticle distance of GNPs also plays a key role in the structural localization of FN protein, and therefore, on the cell attachment behavior. As the distance between the nanoparticles changed from 260 nm (2.75×10^{-3} M) to 160 nm (8.25×10^{-3} M) there was a significant increase in the cell spreading area (Figure 8c). These control surfaces showed cell attachment, but the area covered by cells was significantly lower than their functionalized counterparts. In the case of higher interparticle distances beyond 160 nm, the cell-coverage area was 100 μm^2 (bare) and 260 μm^2 (functionalized). GNPs distance of 160 nm (8.25×10^{-3} M), showed a significant change in cell spreading area from

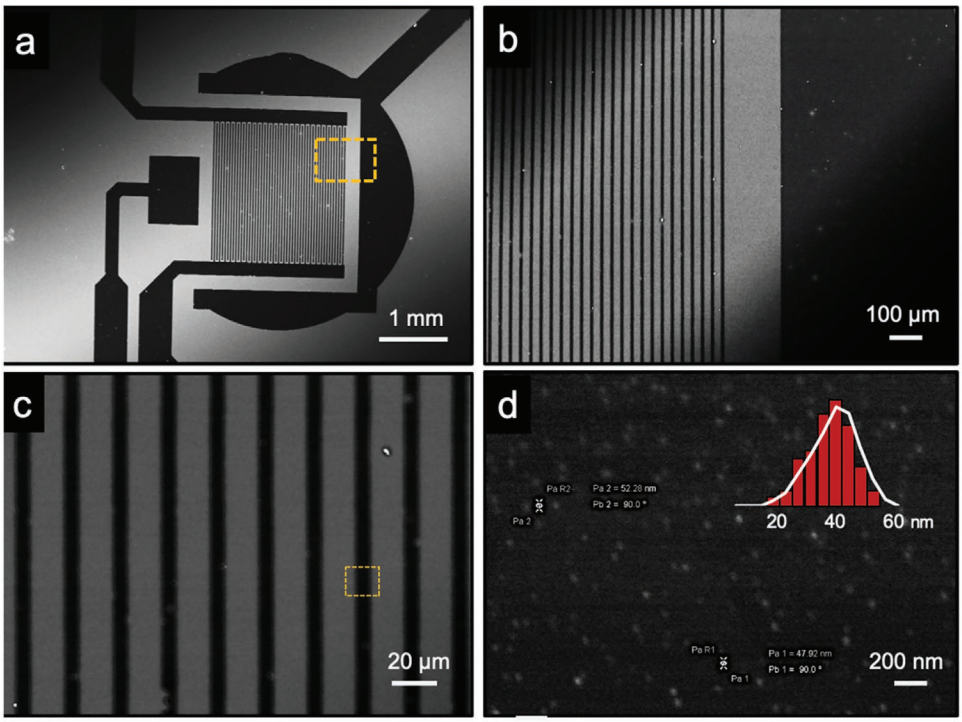

Figure 7. a–c) High definition backscattered electron emission image of GNPs-GC interdigitated electrodes using SU8 formulation with 2 ($NaAuCl_4$, 8.25×10^{-3} M):1 (PI, 4.125×10^{-3} M) molar ratio exposure at 165 mJ cm^{-2}. d) GNPs sized 46 nm (±5 nm) present on the surface of 10 µm feature sized electrodes.

200 μm^2 on control surfaces to 1000 μm^2 for FN-functionalized surfaces. A slight decrease in the cell-coverage area was observed at 50 nm interparticle distance (16.5×10^{-3} M) as compared to the 160 nm (8.25×10^{-3} M) in FN-functionalized surfaces. This may be recognized as a result of steric confinement of cell binding sites present in the adsorbed FN on highly dense GNPs surfaces.

Phalloidin was used to stain the F-actin filaments of the cytoskeleton which are responsible for the interaction between the focal points for cell attachment,[89] whereas Hoechst is used for specifically staining the cell nuclei (**Figure 9**). In the case of GC (control and FN) the cells presented a round morphology which is typical of non-attached cells. Whereas at 2.75×10^{-3} M GNPs concentration (control and FN), the cell number has increased, but as the area of spreading is less the cells are still trying to retain their shape. Surfaces with 8.75 and 16.5×10^{-3} M GNPs (control and FN) both presented large cell-coverage area. Although, cells cultured on FN-functionalized surfaces showed a more spread cell morphology than those cultured on the bare surfaces.

Cell viability and proliferation were also determined at third and eighth day using the LIVE/DEAD assay (**Figure 10**a,b). Cell viability was calculated as the ratio of calcein stained cells (live)/propidium iodide stained cells (dead) at different time points. The GNPs-GC control films showed a cytocompatibility of ≈80% after 3 and 8 days, which was significantly higher than GC control films, which presented 70% viability at the end of both time points. FN functionalization on GNPs-GC surfaces showed an enhanced cell proliferation and well-spread cell morphology. GNPs-GC (8.25×10^{-3} M) and GC (16.5×10^{-3} M) showed an increase in cell proliferation and the cell viability was above 90% in both cases. This makes GNPs-GC a suitable interface for a wide range of biological applications including tissue engineering, molecular electronics, biosensors, and cell and organ chips.

3. Conclusion

To summarize, we developed GC substrates with surface nanospaced GNPs using a fairly simple and scalable process. We presented the details of the various gold nucleation mechanisms involved in the fabrication process, starting from the gold precursor salt reduction in the SU8 photoresist all the way to the final pyrolysis step of the resist at a temperature of 900 °C. Selection of $NaAuCl_4$ over a conventionally used $HAuCl_4$ provides an excellent fabrication control, owing to its great physicochemical compatibility with the photoresist. This detailed understanding of the synthesis process gives the experimenter precise control of GNPs size, distribution, and spacing. The method is generic and other carbon–metal composites can be envisioned upon the proper choice of the metal salt precursor and the pyrolysis process details. Importantly, when exposure dose and resist composition are adapted, the loading of the SU8 photoresist with metal salt precursors does not prevent their patterning and conversion into novel 3D carbon–metal composites structures by pyrolysis.

Cell–material interaction studies on the resultant GNPs-GC surfaces revealed the effect of interparticle spacing of GNPs on cell attachment, cell-coverage area, and cell spreading. In

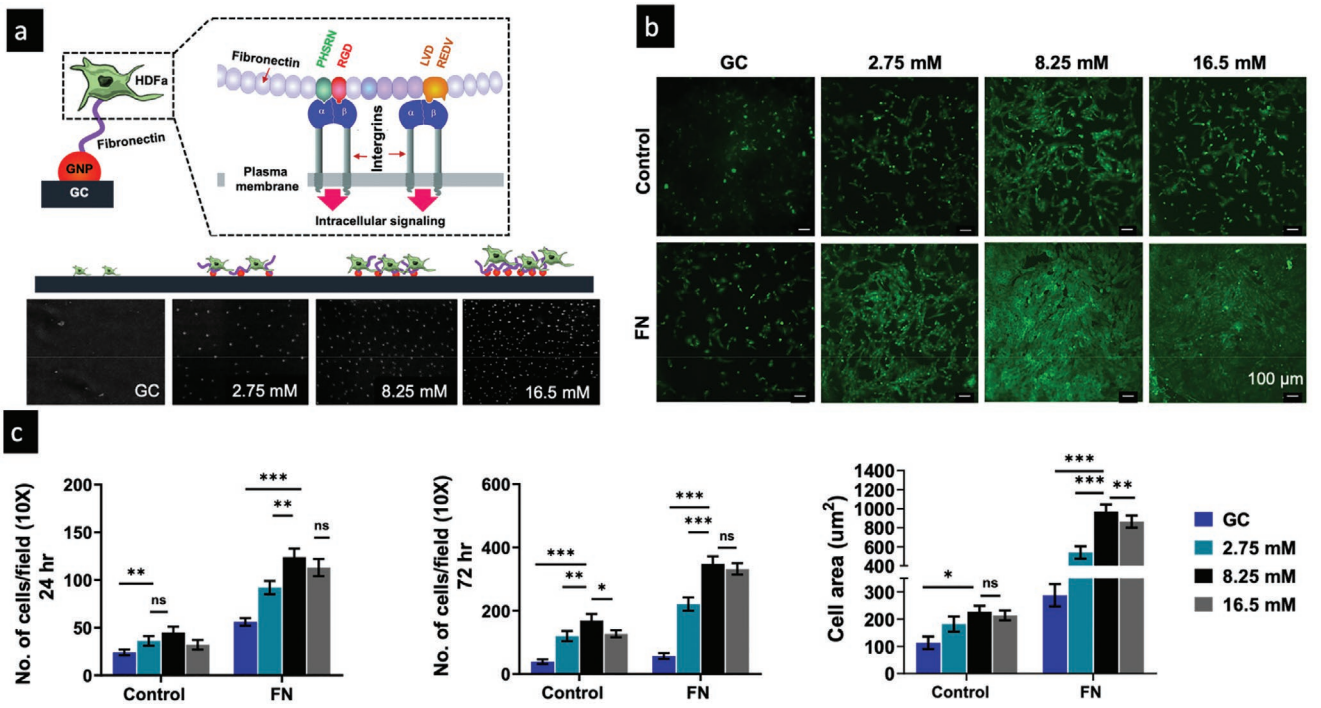

Figure 8. Cell adhesion and proliferation of GFP-HDFa cells. a) Cartoon representing the immobilization of fibronectin on GNPs present on GNPs-GC surface and the attachment mechanism of cell integrin with different fibronectin segments. b) Green florescence of attached and proliferating of GFP-HDFa cells after 48 h, where control represents samples with no fibronectin functionalization. c) Number of attached cells (left and middle graphs) to the bare and functionalized GC and GNPs-GC samples quantified using ImageJ software after 24 and 72 h. Mean cell numbers (±SD) of attached cells from ten random microscopic 10× fields of three independent experiments ($p^* < 0.05$; $^{**}p < 0.01$; $^{***}p < 0.001$). Cell spreading as determined by measuring the cell surface areas (right most graph, $n = 3$ independent experiments, $p^* < 0.05$; $^{**}p < 0.01$; $^{***}p < 0.001$).

general, we observed a trend of increased cell–material interactions when GNPs' concentrations were increased on the substrates, suggesting that GNPs provide physical anchor points to cells for attachment. FN-functionalized surfaces showed an enhanced cell-coverage area, cell proliferation, and cytocompatibility compared to the bare surfaces. As a material for biology and electronics, a variety of micro/nanopatterns could be achieved by lithography-based patterning and controlling the GNPs spacing from a few hundred nanometers to less than 50 nm. This technique will create new opportunities for small molecule, peptide ligand patterns for their application in biosensing, bioelectronics, and lab-on-a-chip system.

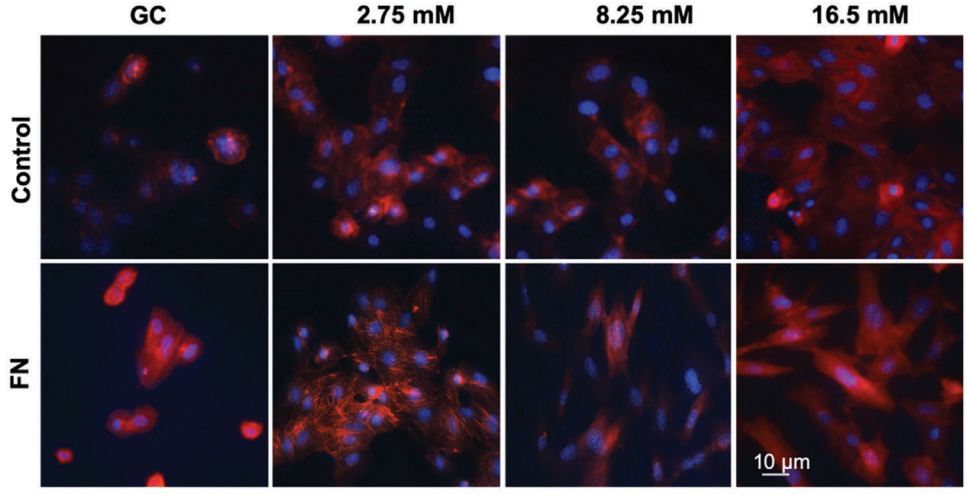

Figure 9. Formation of F-actin stress fibers (stained by phalloidin, red) in human dermal fibroblasts (HDFa) regulated by the density of GNPs on GNPs-GC surface (both control and FN). Hoechst staining (blue) represents the integrity of nuclei of attached cells on different surfaces with or without functionalization.

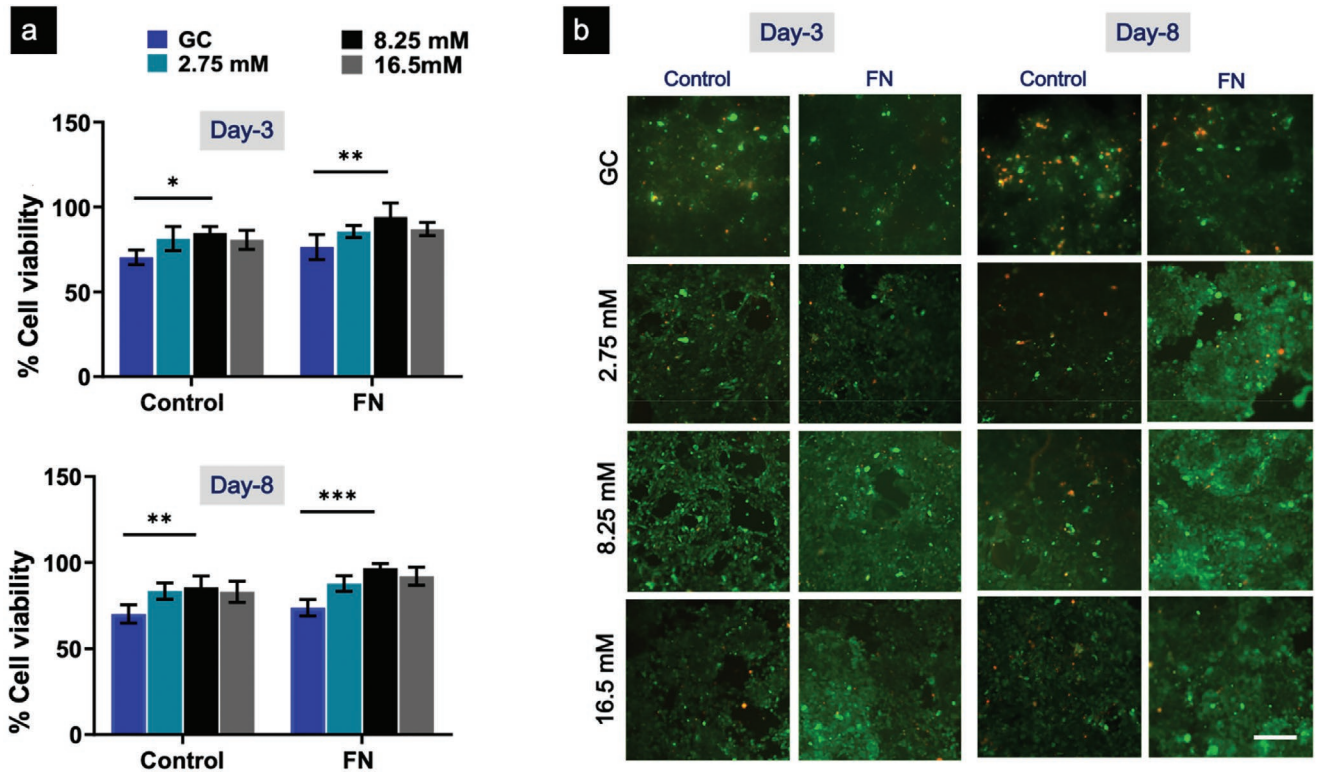

Figure 10. Cell viability assessment of HDFa cells cultured on GNPs-GC surfaces using LIVE/DEAD assay. a) Percentage viable cells grown on bare-control surfaces and FN-functionalized surfaces after third and eighth days ($n = 3$, $p^* < 0.05$; $^{**}p < 0.01$). b) Florescent micrographs of live/dead cell staining after third and eighth days, where calcein stains in green live cells and propidium iodide stains in red dead cells.

4. Experimental Section

Fabrication: With SU8 2007 (MicroChem Corp., USA, density 1.175 g mL^{-1}), different solution concentrations of sodium tetrachloroaurate (III) dehydrate $NaAuCl_4.2H_2O$ (2.75–16.5 × 10^{-3} M) were prepared by dissolving the salt in the photoresist (in amber colored glass vials) with constant magnetic stirring for 120 min at ambient temperature.

Spin coating: Thin film of these precursor solutions was prepared by spin coating on silicon wafers (1.5 × 1.5 cm^2). Standard protocols given in MicroChem data sheet were followed with SU8 mix in order to obtain different film thickness.

Photoresist Crosslinking and Stabilization: First stabilization step for these films was the pre-exposure baking on hot plate for 4 min at 90 °C. Subsequently the films were exposed at 165 mJ cm^{-2} (Dymax 2000-EC). Films were then taken for PEB for 3 min at 90 °C. PEB was followed by hard bake or final cure at a temperature of 200 °C for 1 h.

Pyrolysis: All the stabilized films were pyrolyzed in a furnace (PEO 601, ATV Technologie GmbH, DE) under continuous flow of ultrapure nitrogen at an approximate flow rate of 5.5 L min^{-1}. First, the stabilized samples were heated to 300 °C at a rate of 4.5 °C min^{-1} and maintained at that temperature for 1 h. Next, the temperature was increased to 900 °C at a 2.5 °C min^{-1} ramp rate and held at that temperature for an hour before cooling down to ambient temperature at an approximate rate of 10 °C min^{-1}.

Characterization: The pyrolyzed samples were characterized for the film morphology and GNPs presence on the surface as well as in the cross-section of the thin films, using field emission scanning electron microscopy (FESEM, ZEISS Supra 40VP, Germany) operated at 20 kV voltage. To detect the presence of elemental gold, EDX (Oxford Instruments, England) was performed at 15 kV. XRD (PAN analytical, Germany) was performed from 5° to 80° at a scanning speed of 2° per min to determine the crystallinity of the samples, presence of GNPs, and their crystal structure. Raman spectroscopy was performed with Raman Microscope, equipped with 532-nm excitation laser set, to assess the nature of carbon obtained in the pyrolyzed films. High-resolution transmission electron microscopy (HR-TEM; FEI, Titan 60–300 kV HR/TEM) operated at 300 kV was used to visualize the presence of GNPs in the matrix of the carbon films and to evaluate the microstructure of the pyrolyzed carbon. TEM samples were prepared by drop-casting the finely crushed thin films, suspended in toluene, onto carbon coated copper TEM grids. High-angle annular dark-field imaging (HAADF) was done in STEM mode to analyze the elemental composition of the material. Further the surface characteristics of the pyrolyzed thin films were analyzed using AFM in contact mode on a multimode scanning probe microscope equipped with a Nanoscope IV controller at a scan rate of 5.086 Hz (AFM—AR Instruments, New York, USA). UV–vis absorbance was measured on a UV–vis spectrophotometer (PerkinElmer).

Fibronectin Adsorption: Fibronectin-functionalized surfaces were prepared by the physisorption of the protein on the thin films (1 × 1 cm^2, with a sticky tape on the bottom surface). Films were incubated with 0.5 mg mL^{-1} fibronectin solution (in 0.05 M Tris, 0.5 M NaCl) for 1.5 h at 37 °C. All the surfaces were thoroughly washed (after removing the sticky tape) with double distilled water for 30 min and equilibrated in DMEM-F12 (Dulbecco's Modified Eagle Medium/Nutrient Mixture F-12, Gibco, MA, USA) prior to the experiments. Concentration of fibronectin adsorbed on the surface was further estimated by BCA Protein Assay Kit (Thermo Fisher Scientific, USA).

Cell Culture: For cell experiments, the nanostructured thin films were inserted into 24-well microplates (15.6 mm diameter or 1.9 cm^2 surface area). Primary Dermal Fibroblast; Normal, Human Adult (HDFa) (ATCC PCS-201-012) were grown in DMEM-F12 supplemented with 10% fetal bovine serum (FBS; Gibco, MA, USA). Cells were incubated at 37 °C in a humidified atmosphere containing 5% CO_2. Transfection of plasmid DNA with the GFP gene in HDFa cells was done to study the timely cell

attachment on these opaque substrates. Pure Yield Plasmid Midiprep System Kit (Promega, USA) was initially used to purify plasmid DNA with the GFP gene to transfect the HDFa cells (purified DNA with a concentration of 750 ng μL^{-1}). Lipofectamine 3000 (Invitrogen, CA, USA) was used to transfect the HDFa cells. 24 h before transfection, 2×10^5 cells were seeded in each well of 6-well plates with Opti-MEM (Reduced Serum Media Culture Medium, Gibco, MA, USA). 2.5 µg of DNA (GFP gene, see Figure S5 and Table S1 in the Supporting Information), 250 µL Opti-MEM, 5 µL P3000 and 5 µL Lipofectamine 3000 were used for each well. To generate the liposomes, mix of DNA, P3000, and Lipofectamine 3000 were incubated for 15 min. Finally, the liposomes were added by droplet to the culture in the wells. Transfection was observed after 48 h under fluorescence microscope (Nikon ECLIPSE Ti2, NY, USA) with green florescence of GFP-HDFa cells.

Cell adhesion and Proliferation: GFP-HDFa cells were further grown in T75 flasks were washed with PBS buffer, trypsinized with 0.25% Trypsin-EDTA (Gibco, MA, USA), and collected in DMEM-F12 media. Cells were centrifuged and resuspended in DMEM-12 media with serum proteins/antibiotics. Fibronectin-functionalized films were placed in 24-well plates along with non-functionalized films as control. A suspension of nearly 1×10^5 cells in 1.5 mL of media was placed in each well of the well plate. Cells were then incubated at 37 °C in a humidified atmosphere containing 5% CO_2. All the films were gently washed with PBS buffer before fluorescence microscopy. The number of cells attached and cell area after defined time intervals were analyzed morphometrically using ImageJ software (http://rsb.info.nih.gov/ij/index.html).

Actin filament and Nuclear Staining: HDFa cells suspension of nearly 500 cells in 1.5 mL of media was placed in each well of well plate with nanostructured thin films. Cells were then incubated at 37 °C in a humidified atmosphere containing 5% CO_2 for 48 h. Cells attached to the nanostructured films were washed for 10 min with PBS and fixed with 4% paraformaldehyde for 20 min. Actin filaments (red) were stained with Phalloidin (iFluor 555 reagent, red staining, Abcam, CA, USA) for 30 min and blue emitting nuclear stain Hoechst stain (Invitrogen, H1399) to stain nuclei was added at a final concentrations of 200 nM and 1 µg mL^{-1} in PBS, respectively. After 30 min of incubation, each surface was washed three times and fluorescence images were captured.

Cell Viability Experiment: Nanostructured thin films were incubated with HDFa cells (0.2×10^6 cells per 1.5 mL) in 24-well plates for defined time intervals of 3 days (72 h) and 8 days (192 h), with growth media replaced every 48 h. Calcein AM (Invitrogen, CA, USA) was membrane permeant and can stain both membrane intact or membrane-compromised cells whereas propidium iodide (PI) is only permeable to dead cells/membrane-compromised cells to intercalate with cellular DNA. Fluorescence microscopy pictures were taken using fluorescence microscope to quantify live and dead cell population.

Statistical Analysis: Results were presented as mean ± SD. Significance was calculated using Student's *t*-test or one-way ANOVA with Tukey post hoc test by using SPSS 24.0: $*p < 0.05$, $**p < 0.01$, and $***p < 0.001$. The *p*-value < 0.05 was considered statistically significant.

Supporting Information

Supporting Information is available from the Wiley Online Library or from the author.

Acknowledgements

The authors would like to acknowledge the financial support provided by CONACYT (grant no. CB-2014-1-241458) and the Nano-Sensors and Devices Research Group at Tecnologico de Monterrey (0020209106). Portions of this work were performed at Center for Nanosciences and Advanced Imaging Department, Indian Institute of Technology Kanpur, India. The authors would also like to acknowledge the financial support provided by the Federico Baur Endowed Chair in Nanotechnology (0020240103).

Conflict of Interest

The authors declare no conflict of interest.

Keywords

cell adhesion, glassy carbon, gold nanoparticles, nano-spacing, nucleation

Received: February 11, 2020
Revised: March 13, 2020
Published online: April 19, 2020

[1] J. Lu, S. S. Yi, T. Kopley, C. Qian, J. Liu, E. Gulari, *J. Phys. Chem. B* **2006**, *110*, 6655.
[2] D. A. Boyd, Y. Hao, C. Li, D. G. Goodwin, S. M. Haile, *ACS Nano* **2013**, *7*, 4919.
[3] S. Lal, S. Link, N. J. Halas, *Nat. Photonics* **2007**, *1*, 641.
[4] T. A. Kelf, Y. Tanaka, O. Matsuda, E. M. Larsson, D. S. Sutherland, O. B. Wright, *Nano Lett.* **2011**, *11*, 3893.
[5] S. H. Ko, I. Park, H. Pan, C. P. Grigoropoulos, A. P. Pisano, C. K. Luscombe, J. M. J. Fréchet, *Nano Lett.* **2007**, *7*, 1869.
[6] C. Liu, F. Li, L.-P. Ma, H.-M. Cheng, *Adv. Mater.* **2010**, *22*, E28.
[7] P. Arumugam, S. S. Shinozaki, R. Wang, G. Mao, S. L. Brock, *Chem. Commun.* **2006**, 1121.
[8] Y. Oh, C. Choi, D. Hong, S. D. Kong, S. Jin, *Nano Lett.* **2012**, *12*, 2045.
[9] J. Salber, S. Gräter, M. Harwardt, M. Hofmann, D. Klee, J. Dujic, H. Jinghuan, J. Ding, S. Kippenberger, A. Bernd, J. Groll, J. P. Spatz, M. Möller, *Small* **2007**, *3*, 1023.
[10] N. Perschmann, J. K. Hellmann, F. Frischknecht, J. P. Spatz, *Nano Lett.* **2011**, *11*, 4468.
[11] X. Wang, S. Li, C. Yan, P. Liu, J. Ding, *Nano Lett.* **2015**, *15*, 1457.
[12] R. Glass, M. M ller, J. P. Spatz, *Nanotechnology* **2003**, *14*, 1153.
[13] J. Zheng, Z. Zhu, H. Chen, Z. Liu, *Langmuir* **2000**, *16*, 4409.
[14] J. Chen, P. Mela, M. Möller, M. C. Lensen, *ACS Nano* **2009**, *3*, 1451.
[15] L. G. Donaruma, *J. Polym Sci., Part C: Polym. Lett.* **1988**, *26*, 414.
[16] P. S. Kowalski, C. Bhattacharya, S. Afewerki, R. Langer, *ACS Biomater. Sci. Eng.* **2018**, *4*, 3809.
[17] H. P. Felgueiras, J. C. Antunes, M. C. L. Martins, M. A. Barbosa, in *Peptides and Proteins as Biomaterials for Tissue Regeneration and Repair* (Eds: M. A. Barbosa, M. C. L. Martins), Woodhead Publishing, Sawston, UK **2018**, p. 1.
[18] F. J. O'Brien, *Mater. Today* **2011**, *14*, 88.
[19] K. Amschler, L. Erpenbeck, S. Kruss, M. P. Schön, *ACS Nano* **2014**, *8*, 9113.
[20] T. Bøggild, K. Runager, D. S. Sutherland, *ACS Appl. Mater. Interfaces* **2016**, *8*, 14975.
[21] R. L. McCreery, *Chem. Rev.* **2008**, *108*, 2646.
[22] M. Ghazinejad, S. Holmberg, O. Pilloni, L. Oropeza-Ramos, M. Madou, *Sci. Rep.* **2017**, *7*, 16551.
[23] S. Sharma, C. N. S. Kumar, J. G. Korvink, C. Kubel, *Sci. Rep.* **2018**, *8*, 12.
[24] M. Roushani, F. Shandost-fard, *Anal. Bioanal. Chem. Res.* **2019**, *6*, 13.
[25] M. Bauer, J. Bartoli, S. O. Martinez-Chapa, M. Madou, *Micromachines* **2019**, *10*, 12.
[26] R. Martinez-Duarte, P. Renaud, M. J. Madou, *Electrophoresis* **2011**, *32*, 2385.
[27] L. Farzin, M. Shamsipur, L. Samandari, S. Sheibani, *Microchim. Acta* **2018**, *185*, 25.
[28] A. Salazar, B. Cardenas-Benitez, B. Pramanick, M. J. Madou, S. O. Martinez-Chapa, *Carbon* **2017**, *115*, 811.

[29] B. Hsia, M. S. Kim, M. Vincent, C. Carraro, R. Maboudian, *Carbon* **2013**, *57*, 395.
[30] L. Y. Yu, Q. Zhang, D. Q. Jin, Q. Xu, X. Y. Hu, *Talanta* **2019**, *197*, 622.
[31] H. S. Yin, Q. M. Zhang, Y. L. Zhou, Q. A. Ma, T. Liu, L. S. Zhu, S. Y. Ai, *Electrochim. Acta* **2011**, *56*, 2748.
[32] J. Zou, G. Q. Zhao, J. Teng, Q. Liu, X. Y. Jiang, F. P. Jiao, J. G. Yu, *Microchem. J.* **2019**, *693*, 145.
[33] R. Perveen, Inamuddin, A. Nasar, Beenish, A. M. Asiri, *Int. J. Biol. Macromol.* **2018**, *106*, 755.
[34] S. Y. Wu, J. L. Chen, D. L. Liu, Q. Zhuang, Q. Pei, L. X. Xia, Q. Zhang, J. Kikuchi, Y. Hisaeda, X. M. Song, *RSC Adv.* **2016**, *6*, 70781.
[35] Y. Fang, Y. L. Ni, G. H. Zhang, C. Mao, X. H. Huang, J. Shen, *Bioelectrochemistry* **2012**, *88*, 1.
[36] W. da Silva, M. E. Ghica, R. F. Ajayi, E. I. Iwuoha, C. M. A. Brett, *Food Chem.* **2019**, *282*, 18.
[37] S. V. Fischer, B. Uthuppu, M. H. Jakobsen, *Beilstein J. Nanotechnol.* **2015**, *6*, 1661.
[38] S. Shukla, X. Vidal, E. P. Furlani, M. T. Swihart, K.-T. Kim, Y.-K. Yoon, A. Urbas, P. N. Prasad, *ACS Nano* **2011**, *5*, 1947.
[39] V. Biju, *Chem. Soc. Rev.* **2014**, *43*, 744.
[40] J. J. Park, X. Bulliard, J. M. Lee, J. Hur, K. Im, J. M. Kim, P. Prabhakaran, N. Cho, K. S. Lee, S. Y. Min, T. W. Lee, S. Yong, D. Y. Yang, *Adv. Funct. Mater.* **2010**, *20*, 2296.
[41] M. Vafaiee, M. Vossoughi, R. Mohammadpour, P. Sasanpour, *Sci. Rep.* **2019**, *9*, 11.
[42] G. Chauhan, V. Chopra, A. Tyagi, G. Rath, R. K. Sharma, A. K. Goyal, *Eur. J. Pharm. Sci.* **2017**, *96*, 351.
[43] T. Malik, G. Chauhan, G. Rath, R. N. Kesarkar, A. S. Chowdhary, A. K. Goyal, *Artif. Cells, Nanomed., Biotechnol.* **2018**, *46*, 79.
[44] C. Matricardi, C. Hanske, J. L. Garcia-Pomar, J. Langer, A. Mihi, L. M. Liz-Marzan, *ACS Nano* **2018**, *12*, 8531.
[45] F. Pu, X. Ran, M. Guan, Y. Y. Huang, J. S. Ren, X. G. Qu, *Nano Res.* **2018**, *11*, 3213.
[46] J. S. Chae, N. S. Heo, C. H. Kwak, W. S. Cho, G. H. Seol, W. S. Yoon, H. K. Kim, D. J. Fray, A. T. E. Vilian, Y. K. Han, Y. S. Huh, K. C. Roh, *Nano Energy* **2017**, *34*, 86.
[47] N. German, A. Ramanavicius, A. Ramanaviciene, *Sens. Actuators, B* **2014**, *203*, 25.
[48] G. Gotti, K. Fajerwerg, D. Evrard, P. Gros, *Electrochim. Acta* **2014**, *128*, 412.
[49] M. Khater, A. de la Escosura-Muniz, D. Quesada-Gonzalez, A. Merkoci, *Anal. Chim. Acta* **2019**, *1046*, 123.
[50] S. R. Ahmed, J. Kim, V. T. Tran, T. Suzuki, S. Neethirajan, J. Lee, E. Y. Park, *Sci. Rep.* **2017**, *7*, 11.
[51] S. S. Tzeng, *Carbon* **2006**, *44*, 1986.
[52] Z. H. Huang, H. H. Zhou, Q. L. Peng, J. H. Chen, Y. F. Kuang, *Trans. Nonferrous Met. Soc. China* **2010**, *20*, 1418.
[53] A. B. Garcia, I. Camean, J. L. Pinilla, I. Suelves, M. J. Lazaro, R. Moliner, *Fuel* **2010**, *89*, 2160.
[54] S. Shukla, E. P. Furlani, X. Vidal, M. T Swihart, P. N. Prasad, *Adv. Mater.* **2010**, *33*, 3695.
[55] J. P. Markham, S. T. Staben, F. D. Toste, *J. Am. Chem. Soc.* **2005**, *127*, 9708.
[56] W. J. Peveler, I. P. Parkin, *RSC Adv.* **2013**, *3*, 21919.
[57] N. T. K. Thanh, N. Maclean, S. Mahiddine, *Chem. Rev.* **2014**, *114*, 7610.
[58] T. Sugimoto, *Adv. Colloid Interface Sci.* **1987**, *28*, 65.
[59] T. Sugimoto, *Monodispersed particles*, Elsevier Science, Amsterdam **2001**.
[60] V. K. LaMer, R. H. Dinegar, *J. Am. Chem. Soc.* **1950**, *72*, 4847.
[61] S. Kundu, A. Pal, S. K. Ghosh, S. Nath, S. Panigrahi, S. Praharaj, T. Pal, *Inorg. Chem.* **2004**, *43*, 5489.
[62] G. Frens, *Nature* **1973**, *241*, 20.
[63] J. Turkevich, P. C. Stevenson, J. Hillier, *Discuss. Faraday Soc.* **1951**, *11*, 55.
[64] J. Kimling, M. Maier, B. Okenve, V. Kotaidis, H. Ballot, A. Plech, *J. Phys. Chem. B* **2006**, *110*, 15700.
[65] T. Yao, Z. H. Sun, Y. Y. Li, Z. Y. Pan, H. Wei, Y. Xie, M. Nomura, Y. Niwa, W. S. Yan, Z. Y. Wu, Y. Jiang, Q. H. Liu, S. Q. Wei, *J. Am. Chem. Soc.* **2010**, *132*, 7696.
[66] X. H. Ji, X. N. Song, J. Li, Y. B. Bai, W. S. Yang, X. G. Peng, *J. Am. Chem. Soc.* **2007**, *129*, 13939.
[67] M. K. Chow, C. F. Zukoski, *J. Colloid Interface Sci.* **1994**, *165*, 97.
[68] V. K. LaMer, *Ind. Eng. Chem.* **1952**, *44*, 1270.
[69] S. G. Kwon, T. Hyeon, *Small* **2011**, *7*, 2685.
[70] J. Polte, *CrystEngComm* **2015**, *17*, 6809.
[71] I. Gibson, D. Rosen, B. Stucker, *Additive Manufacturing Technologies: 3D Printing, Rapid Prototyping, and Direct Digital Manufacturing*, Springer, Berlin **2015**.
[72] R. Martinez-Duarte, M. J. Madou, in *Microfluidics and Nanofluidics Handbook: Fabrication, Implementation, and Applications*, CRC Press-Taylor & Francis Group, Boca Raton, FL **2012**, p. 231.
[73] J. Wang, H. F. M. Boelens, M. B. Thathagar, G. Rothenberg, *ChemPhysChem* **2004**, *5*, 93.
[74] D. A. Poeter, K. E. Easterling, *Phase Transformations in Metals and Alloys*, Chapman & Hall, London **1992**.
[75] Q. Hu, X. Z. Sun, C. D. J. Parmenter, M. W. Fay, E. F. Smith, G. A. Rance, Y. F. He, F. Zhang, Y. Liu, D. Irvine, C. Tuck, R. Hague, R. Wildman, *Sci. Rep.* **2017**, *7*, 9.
[76] W. Ostwald, *Zeitschrift für Physikalische Chemie* **1897**, *22*, 289.
[77] H. M. Zheng, R. K. Smith, Y. W. Jun, C. Kisielowski, U. Dahmen, A. P. Alivisatos, *Science* **2009**, *324*, 1309.
[78] X. G. Peng, J. Wickham, A. P. Alivisatos, *J. Am. Chem. Soc.* **1998**, *120*, 5343.
[79] M. D. Clark, S. K. Kumar, J. S. Owen, E. M. Chan, *Nano Lett.* **2011**, *11*, 1976.
[80] W. R. Lee, M. G. Kim, J. R. Choi, J. I. Park, S. J. Ko, S. J. Oh, J. Cheon, *J. Am. Chem. Soc.* **2005**, *127*, 16090.
[81] A. La Torre, M. D. Gimenez-Lopez, M. W. Fay, G. A. Rance, W. A. Solomonsz, T. W. Chamberlain, P. D. Brown, A. N. Khlobystov, *ACS Nano* **2012**, *6*, 2000.
[82] I. Lifshitz, *J. Phys. Chem. Solids* **1961**, *19*, 35.
[83] C. Wagner, *Z. Elektrochem.* **1961**, *65*, 581.
[84] T. van Westen, R. D. Groot, *Cryst. Growth Des.* **2018**, *18*, 4952.
[85] K. Dick, T. Dhanasekaran, Z. Y. Zhang, D. Meisel, *J. Am. Chem. Soc.* **2002**, *124*, 2312.
[86] R. Natu, M. Islam, J. Gilmore, R. Martinez-Duarte, *J. Anal. Appl. Pyrolysis* **2018**, *131*, 17.
[87] M. J. Madou, *Fundamentals of Microfabrication and Nanotechnology*, CRC Press, Boca Raton, FL.
[88] J. A. Deeg, I. Louban, D. Aydin, C. Selhuber-Unkel, H. Kessler, J. P. Spatz, *Nano Lett.* **2011**, *11*, 1469.
[89] R. Lutz, K. Pataky, N. Gadhari, M. Marelli, J. Brugger, M. Chiquet, *PLoS One* **2011**, *6*, e25459.